


RESEARCH

Open Access



Spatial relationships and interactions of immune cell niches are linked to the pathologic response of muscle-invasive bladder cancer to neoadjuvant therapy

Wasilijiang Wahafu^{1,2}, Quan Zhou³, Xihua Yang⁴, Yongming Yang⁴, Yuanyuan Zhao⁵, Zhu Wang², Xiangpeng Kang², Xiongjun Ye¹ and Nianzeng Xing^{1,2*} 

Abstract

Background The identification of the complex spatial architecture of immune cell infiltration and its interaction mechanisms within tumor ecosystems provides crucial insights into therapeutic responses to neoadjuvant therapy in muscle-invasive bladder cancer (MIBC). This study aims to characterize the spatial features of distinct cell-type niches within the tumor microenvironment (TME) of patients with varying responses to neoadjuvant therapy.

Methods We performed spatial transcriptomic profiling on six MIBC specimens obtained from a registered clinical trial (ChiCTR2000032359), generating whole-transcriptome spatial atlases to map the TME architecture. High-throughput analytical frameworks were employed to deconstruct the TME, and key findings were validated through immunohistochemistry and mouse model experiments.

Results Our analysis revealed that tissues from complete responders exhibited greater infiltration of T and B cells, with the formation of tertiary lymphoid structure (TLS). Trajectory analysis identified CCL19/CCL21 as the key signaling molecules driving TLS formation in MIBC. Mouse experiments demonstrated that recombinant CCL19/CCL21 protein injections promoted intratumoral TLS formation and enhance the efficacy of immunotherapy. Furthermore, we observed significant intrinsic heterogeneity within individual tumors, which may contribute to the lack of therapeutic efficacy in MIBC.

Conclusions This study underscores the critical role of TLS formation in the response to neoadjuvant therapy in MIBC. We identified CCL19/CCL21 as key drivers of TLS formation within MIBC tumors and potential immune-sensitizing agents. Additionally, the intrinsic heterogeneity of tumor should be considered a significant factor influencing therapeutic efficacy.

Keywords Bladder cancer, Neoadjuvant therapy, Spatial transcriptomics, Tertiary lymphoid structures, Immune cell niche

*Correspondence:

Nianzeng Xing
xingnianzeng@126.com

Full list of author information is available at the end of the article



© The Author(s) 2025. **Open Access** This article is licensed under a Creative Commons Attribution-NonCommercial-NoDerivatives 4.0 International License, which permits any non-commercial use, sharing, distribution and reproduction in any medium or format, as long as you give appropriate credit to the original author(s) and the source, provide a link to the Creative Commons licence, and indicate if you modified the licensed material. You do not have permission under this licence to share adapted material derived from this article or parts of it. The images or other third party material in this article are included in the article's Creative Commons licence, unless indicated otherwise in a credit line to the material. If material is not included in the article's Creative Commons licence and your intended use is not permitted by statutory regulation or exceeds the permitted use, you will need to obtain permission directly from the copyright holder. To view a copy of this licence, visit <http://creativecommons.org/licenses/by-nc-nd/4.0/>.

Introduction

Bladder cancer is the ninth most frequently diagnosed cancer in the world [1]. Neoadjuvant cisplatin-based chemotherapy, administered prior to radical cystectomy, has been shown to improve survival in patients with muscle-invasive bladder cancer (MIBC). However, only 30% of patients achieve a pathological complete response (pCR) following radical surgery [2]. In recent years, neoadjuvant therapy with single-agent immune checkpoint inhibitors (ICIs) has demonstrated pCR rates of 30–40% in MIBC patients. Given that cisplatin may induce favorable immunomodulatory effects [3], several phase II clinical trials have explored ICI-chemotherapy combination regimens, resulting in pCR rates ranging from 40–50% [4, 5]. Although combination therapies have enhanced the sensitivity of immunotherapy, the underlying interaction mechanisms within the tumor microenvironment (TME) is still unknown.

Advances in single-cell RNA sequencing (scRNA-seq) technology have significantly enhanced our understanding of the TME at the individual cell level [6]. However, a major limitation to scRNA-seq is the loss of spatial and morphological context when tissues are dissociated into single cells, which complicates the study of tumor architecture. While in situ hybridization (ISH)-based techniques, such as multiple error-robust fluorescence in situ hybridization (MERFISH) [7] and sequential fluorescence in situ hybridization (seqFISH) [8], are capable of providing spatial information, they are limited by the number of target genes that can be analyzed simultaneously. The recently developed and widely adopted spatial transcriptomics (ST) technology offers a promising solution to these limitations, enabling the study of spatial gene expression at a tissue-wide scale [9].

In this study, we investigated the spatial transcriptomic architecture of MIBC to identify TME characteristics that contribute to the response to neoadjuvant therapy. Our findings indicate that patients who achieved a pCR exhibited a high degree of lymphocytic infiltration, immune activation, and TLS formation at the naïve stage of treatment. Additionally, we identified intrinsic heterogeneity within individual tumors, which was found to correlate with tumor's response to neoadjuvant therapy. These results provide new insights into the complex ecosystem of MIBC and offer potential strategies for enhancing the efficacy of precision medicine in treating MIBC.

Materials and methods

Human MIBC samples

This study enrolled eight patients diagnosed with MIBC at the Cancer Hospital, Chinese Academy of Medical Sciences and Peking Union Medical College. Pretreatment samples were obtained from patients who consented

to participate in a clinical trial, which is registered at <https://www.chictr.org.cn> (ChiCTR2000032359) [4]. Prior to surgery, all patients were informed about the potential use of their pathological specimens for medical research and provided written informed consent. After diagnostic transurethral resection of bladder tumors (TURBT), patients received three cycles of camrelizumab in combination with gemcitabine and cisplatin as neoadjuvant therapy. Each treatment cycle consisted of 200 mg camrelizumab administered intravenously (IV) once on day 1, 1000 mg/m² gemcitabine IV once on days 1 and 8, and 70 mg/m² cisplatin IV once on day 2, administered every 3 weeks. Radical cystectomy (RC) was performed 3–4 weeks after the completion of neoadjuvant therapy.

Among the 8 patients enrolled, the patients were classified into two groups based on their tumor response to neoadjuvant therapy: 5 patients with complete response (CR) and 3 patients with non-CR. Additionally, paired treatment-naïve and treatment-experienced formalin-fixed paraffin-embedded (FFPE) sections from 3 patients were included for further analysis, with the following classifications: progressive disease (PD) (n=1), stable disease (SD) (n=1), and CR (n=1).

ST sequencing

The RNA quality of FFPE tissue blocks was evaluated by calculating the DV200 of RNA extracted from FFPE tissue sections, following the protocol provided by the Qiagen RNeasy FFPE Kit. Five-micron-thick tissue sections were mounted on a Sigma-Aldrich Poly Prep Slide in accordance with the Visium CytAssist Spatial Gene Expression Protocols for FFPE-Tissue Preparation Guide (10×Genomics, CG000518 Rev C). After drying overnight, the slides were incubated at 60 °C for 2 h. Deparaffinization was then performed following the Visium CytAssist Spatial Gene Expression for FFPE Samples-Deparaffinization, Decrosslinking, Immunofluorescence Staining & Imaging Protocol (10×Genomics, CG000519 Rev B). The tissue sections were stained with haematoxylin and eosin (H&E) and imaged at 20× magnification via brightfield imaging using a Leica Aperio Versa8 whole-slide scanner. Decrosslinking was then performed immediately on H&E-stained sections. Next, human whole-transcriptome probe panels were added to the tissue. After these probe pairs hybridized to their target genes and were ligated to one another, the slides were placed on a Visium CytAssist instrument for RNase treatment and permeabilization. The ligated probes were then hybridized to the spatially barcoded oligonucleotides in the capture area. Spatial transcriptomics libraries were generated from the probes and sequenced on the Illumina NovaSeq 6000 system (performed by Beijing Novogene Technology Co., Ltd.). After cDNA library

construction and sequencing, we used an in-house script to perform a basic statistical analysis of the raw data and to evaluate the data quality and GC content throughout the sequencing cycles. Raw FASTQ files and histology images were processed via the short-read probe alignment algorithm for the FFPE ‘count’ method in Space Ranger (v1.3.0) from 10× Genomics to align probe reads to the human reference genome (GRCh38/mm10). The filtered count matrix and the fiducial-aligned low-resolution image were used for downstream data analyses using the R package Seurat (v.4.0.4).

H&E and immunohistochemistry

FFPE sections of MIBC were obtained from the clinical trial ChiCTR2000032359. A representative slide from each patient was stained with H&E. For immunohistochemistry (IHC), the MIBC tissue sections were stained with the following primary antibodies: anti-CD3 (Abcam, ab16669), anti-CD20 (Abcam, ab78237), anti-PNAd (BD Biosciences, 553863), anti-GATA3 (Abcam, ab199428), anti-ACTA2 (Thermo Fisher, 14–9760-82), anti-PEG10 (Novus, NBP2-13749), anti-FGFR3 (Thermo Fisher, 66954-1-IG) and anti-CK5/6 (NSJ Bioreagents, V8493-20UG). For the murine samples, sections were stained with anti-CD3 (Abcam, ab16669) and anti-CD19 (CST, 90176 T) antibodies.

TLS identification and quantification

We used the following criteria for the identification of TLSs: (1) Aggregations of large numbers of T cells and B cells; (2) Exhibits distinct T cell zone and B cell zones; (3) Presence of high endothelial venules (HEVs) in the surrounding of T cell zone and B cell zone. We performed quantitative analysis based on the TLS area and the TLS number per 1 mm² of tumor tissue. The “ratio of TLS/mm²” was calculated as the total area of all TLS in each tumor section divided by the area of the tumor tissue. The “number of TLS/mm²” was calculated as the total number of TLS in each tumor section divided by the area of the tumor tissue.

ST data preprocessing

The ST data were processed using the R programming language. Quality control for each of the six samples was performed individually using the default Seurat pipeline. We identified 3000 high variable features (HVF) according to their expression means and variances and finally obtained common HVFs among the six samples from 3 patients (one PD, one SD and one CR patients respectively) for further analysis. The data from all six samples were then merged, followed by normalization, scaling, and principal component analysis (PCA). Integration and batch correction were performed using the

harmony method with default parameters. Unsupervised clustering based on shared nearest neighbour (SNN) was applied to the spots, and the clustering results were visualized using (t-distributed stochastic neighbor embedding) t-SNE. Finally, these clusters were annotated based on canonical cell type markers.

Statistical analysis

The TLS quantification and mouse experiments data were presented as the mean ± SEM and analyzed using GraphPad Prism 10 software. Differences between groups were determined by Student’s t-tests. For downstream analysis of ST data, the differential expression analysis among the PD, SD, and CR groups was performed using the FindAllMarkers function of the Seurat package. The results were visualized as volcano plots with the ggplot2 package. Differentially expressed genes were determined by a p-value ≤ 0.05 and a |log₂FC| ≥ 1. Gene Ontology (GO) and gene set variation analysis (GSVA) were conducted with the clusterProfiler and GSVA packages under default parameters. To explore the temporal progression of TLS formation, a pseudotime analysis was conducted using the Monocle2 tools. Dominant ligand-receptor pairs in the TLS regions were identified using the SpaGene method with the default parameters. The downstream analysis of ST data was conducted by R software (<https://www.R-project.org/>) v4.1.0.

Cell culture, mice and preclinical experiments

The mouse urothelial carcinoma cell line MB49 was procured from Shanghai Fuheng Biotechnology Company (www.fudancell.com) and cultured in Dulbecco’s Modified Eagle Medium (DMEM) supplemented with 10% (v/v) fetal bovine serum (FBS) (Shanghai Fuheng Biotechnology Company, FH1136). 6- to 8 week-old wild-type C57BL/6 J mice were obtained from SiPeiFu, Inc. (<https://www.spfbiotech.com>) and maintained under specific pathogen-free conditions. To establish a xenograft tumor model, the mice were intraperitoneally injected with 4 × 10⁵ MB49 cells. A mixture of 1.5 µg of Ccl19 (PeproTech, cat: 250-27B-20UG) and 1.5 µg of Ccl21 (PeproTech, cat: 250-13-20UG) was administered intraperitoneally on days 3, 5, and 7 after tumors were visible on the mice, and 250 µg of anti-mouse PD-1 (BioXcell, cat: BE0146) or 250 µg of anti-mouse IgG2a isotype (BioXcell, cat: BE0089) was administered intraperitoneally on days 10, 12, and 14 after tumors were visible. On day 17, after tumors were visible, the mice were sacrificed, and the final tumor weight was measured.

Ethics

This study was conducted in accordance with the principles of the Declaration of Helsinki. The use of patient

samples was approved by the National Cancer Center/Cancer Hospital, Chinese Academy of Medical Sciences and Peking Union Medical College (approval #20/084–2280). Informed consent was obtained from all patients prior to inclusion in the study. All animal experiments were also approved by the Shanxi Province Cancer Hospital/Shanxi Hospital Affiliated to Cancer Hospital, Chinese Academy of Medical Sciences/Cancer Hospital Affiliated to Shanxi Medical University (approval #2023KJT33) and were performed in compliance with institutional and national guidelines for the care and use of laboratory animals.

Role of funders

The study funders had no role in the study design, data collection, data analysis, data interpretation, manuscript writing, or in the decision to submit the manuscript for publication.

Results

TLS are enriched in patients who achieve CR

To examine the lymphocytic context in MIBC prior to neoadjuvant therapy, we assessed T-cell and B-cell infiltration using IHC on tissue sections obtained via electrotomy, including treatment-naïve samples from patients enrolled in a clinical trial (ChiCTR2000032359) patients with non-CR ($n=3$) and CR ($n=5$) responses [4]

(Fig. 1A). Our analysis revealed that the CR group exhibited a higher density of T/B-cell clustered structures, alongside numerous co-distributed HEVs, indicative of the presence of TLS structures (Fig. 1B, C). Quantitative analysis of the IHC maps demonstrated that the density of TLSs in tissues from patients who achieved CR was significantly higher compared to those from non-CR patients (Fig. 1D).

Spatial heterogeneities of the cell-type niche in the MIBC microenvironment

To further explore the spatial heterogeneity of the TME in CR and non-CR patients and to analyze the transcriptional characteristics of TLSs, we employed Visium ST technology from 10X Genomics. ST was performed on paired treatment-naïve and treatment-experienced FFPE sections from three patients in our cohort, including those with PD ($n=1$), SD ($n=1$), and CR ($n=1$), generating six spatial expression maps (Fig. 2A). Following quality control, a total of 20,020 spots from these maps were retained for subsequent analysis. To characterize the spatial diversity of cell-type niche (CTN) within the MIBC TME, we combined the spots from different tissues and performed clustering analysis (Fig. 2B). Eight distinct CTNs were identified based on canonical cell-type markers and signatures. These included T/B cells (Immune/TB), myeloid cells (Immune/myeloid), immune cell

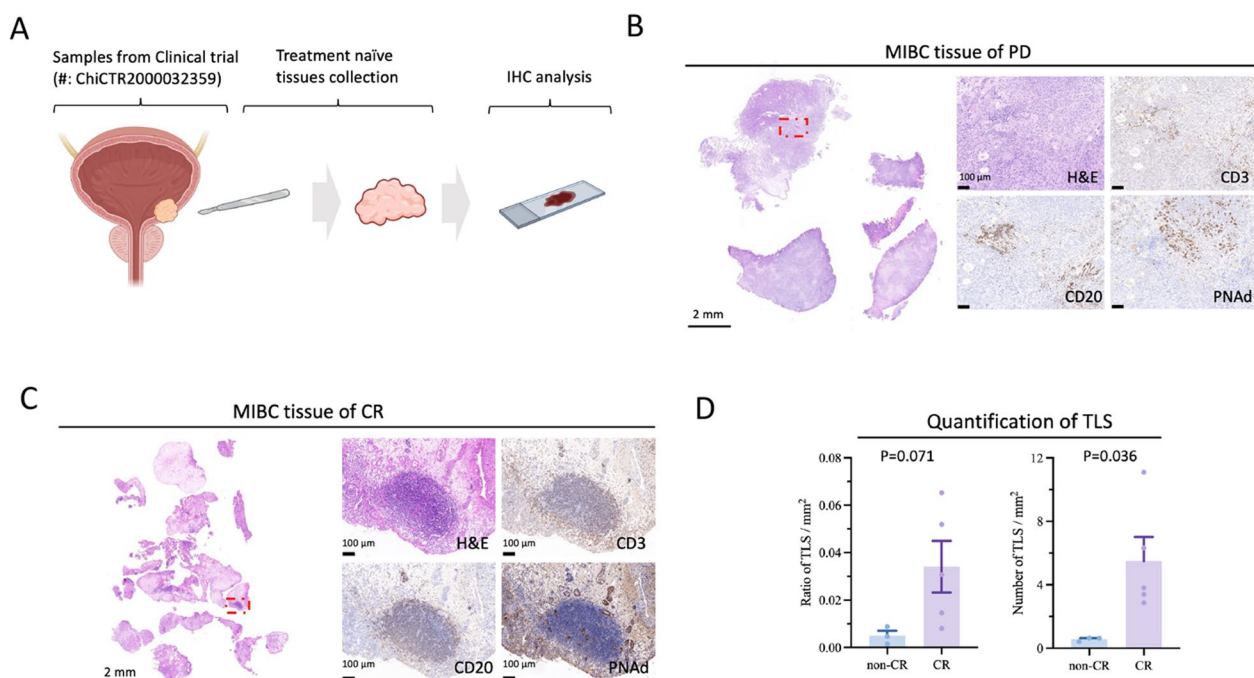


Fig. 1 Treatment naïve tumor tissues of CR patients are enriched with TLSs. **A** Electrotomy tissues of MIBC were collected from patients enrolled in clinical trials. **B–C** TLS was defined by H&E and immunohistochemical staining for CD3, CD20 and PNAd. **D** Quantitative analysis of TLS. The difference between group was analyzed by Student's t-tests. $n=3$ patients for non-CR, $n=5$ for CR

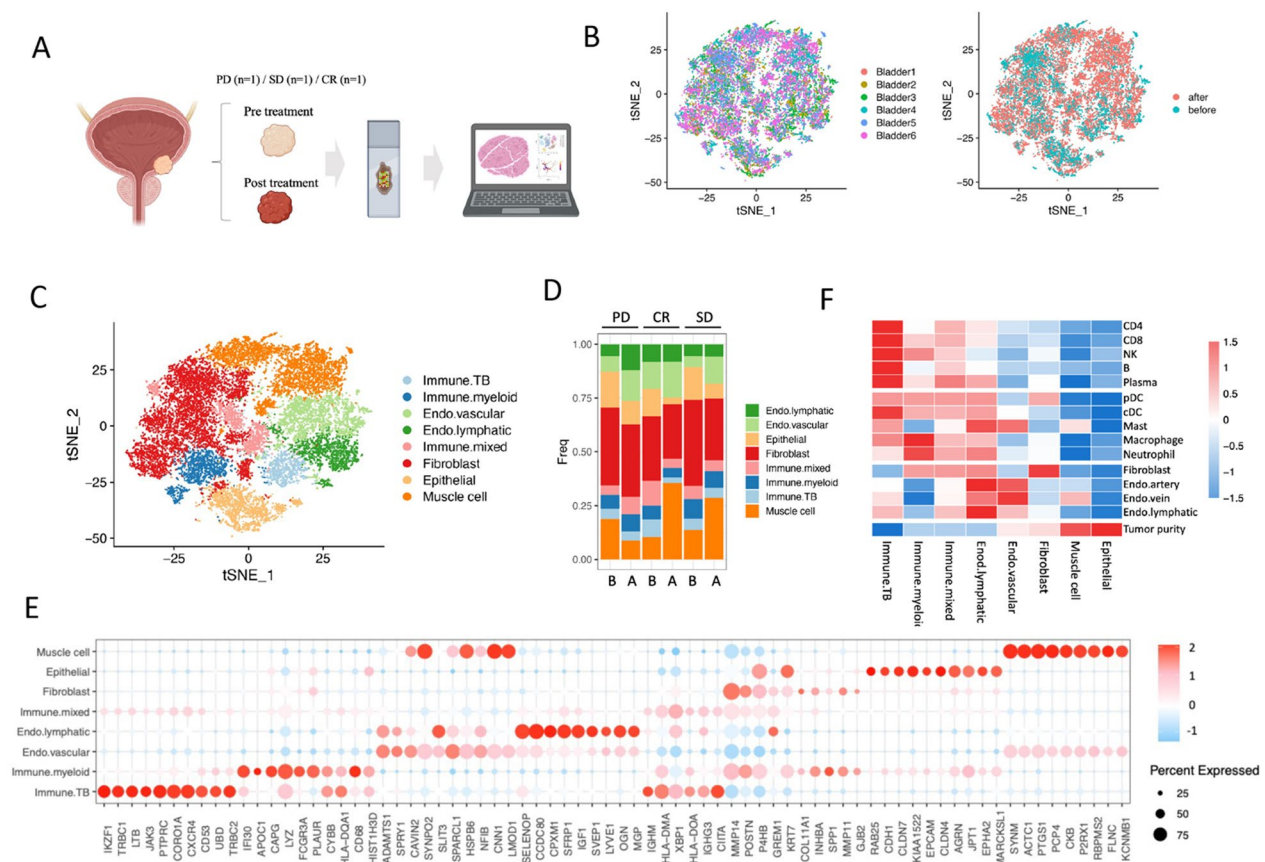


Fig. 2 Characterization of cell-type niche diversity in MIBC. **A** Spatial transcriptome sequencing was conducted with pre- and post-treatment tumor section of three patients. The graph was generated by Biorender (<https://biorender.com>). **B** tSNE map of all spots (20,020) in MIBC dataset colored by sample names and treatment group. **C** tSNE map of all spots in MIBC dataset colored by cell-type niches. **D** Proportion of cell-type niches in each sample (**B**: before treatment, **A**: after treatment). **E** Dotplot shows feature genes of cell-type niche. **F** Heatmap shows signature score of cell types in cell-type niches

mixtures (Immune/mixed), vascular vessels (Endovascular), lymphatic vessels (Endolymphatic), and fibroblast, epithelial and muscle cell-enriched niches (Fig. 2C, Fig. S1). All types of CTNs can be observed in the individual maps (Fig. 2D, Fig. S2), and the identification of specific markers of CNTs further validated the accuracy of the clustering analysis (Fig. 2E). Notably, the tumor purity signal was highly enriched in the epithelial and muscle cell niches, which is consistent with the pathological phenotype of MIBC (Fig. 2F).

Patients in the CR group present increased lymphocyte infiltration and activation

To further explore the neoadjuvant therapy-associated immune niches, we compared the abundance of CTNs between treatment-naïve tissues from patients who achieved a CR and those who did not, using the odds ratio test (Fig. 3A). We found that immune-related CTNs, such as Immune/TB, Immune/mixed,

and endothelial-associated niches, were significantly enriched in the tissues from CR patients (Fig. 3A, B). Enhanced lymphocytic infiltration is known to contribute to better responses to immunotherapy, while an increased density of blood vessels aids in the efficient delivery of chemotherapy agents. We then compared the Immune/TB and Immune/mixed niches between CR and non-CR tissues through differential gene expression analysis (Fig. 3C). The CR group exhibited higher expression of several B-cell-related genes, including MS4A1, CD79A, BANK1, BLK, and FCRL1 (Fig. 3C). GO analysis revealed that the differentially expressed genes (DEGs) from both the Immune/TB and Immune/mixed niches were primarily involved in adaptive immune-related biological processes, particularly those associated with B-cell function (Fig. 3D, E). Moreover, we observed an increased expression of genes related to B-cell activation in CR tissues,

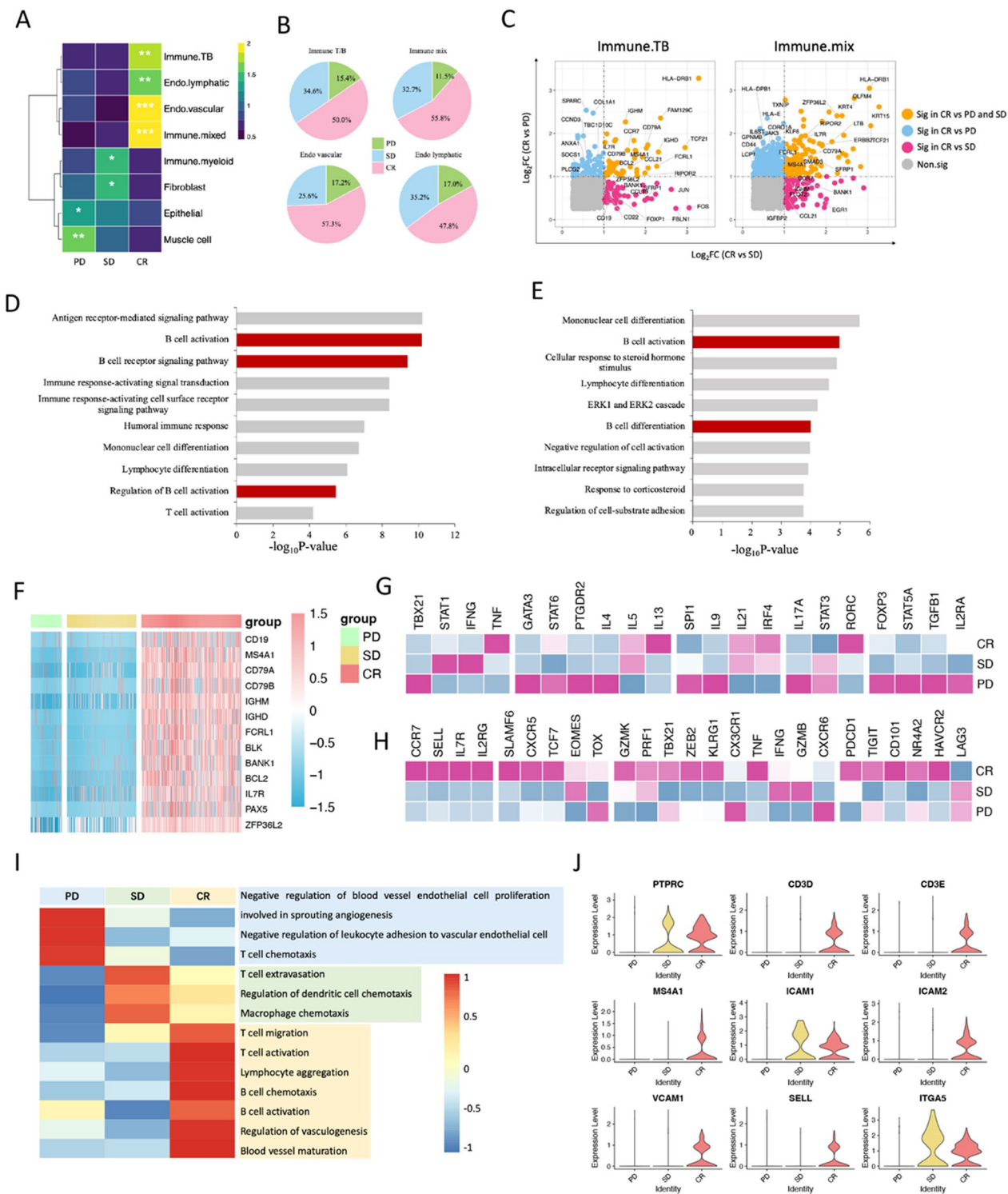


Fig. 3 The pre-treatment tissues of CR patients exhibit increased lymphocyte infiltration and activation. **A** Heatmap shows odd ratios of cell-type niches in pre-treatment tissues. **B** Pie-plots shows the proportion of the spots of Immune.TB, Immune.mix, Endo.vascular and Endo.lymphocyte origins across difference response tissues. **C** Volcano plots shows differential expressed genes between indicated groups. **D** GO analysis identified the biological processes that co-significant genes of Immune.TB involved in. **E** GO analysis identified the biological processes that co-significant genes of Immune.mix involved in. **F** Heatmap shows the expression of genes that involved in B cell activation. **G** Heatmap shows the expression of CD4 T cell subtype markers in CD4 T cell spots. **H** Heatmap shows the expression of CD8 T cell subtype markers in CD8 T cell spots. **I** GSEA analysis identified the biological processes involved by differential expressed genes in Endo.vascular niche across different response groups. **J** Violin plots show the expression of lymphocyte and adhesion molecular markers across different response groups

suggesting that B-cell-mediated immunity may play a critical role in the response to neoadjuvant therapy (Fig. 3F).

T cells undergo functional polarization, which is largely influenced by the TME [10, 11]. We hypothesized that infiltrating T cells in response to different treatment regimens would exhibit distinct phenotypes and functional statuses. To test this hypothesis, we extracted T-cell spots (defined as spots expressing both CD3 and either CD4 or CD8) and assessed T-cell populations in the different treatment-response groups based on the expression levels of T-cell subtype and activation-related marker genes. As anticipated, regulatory T cells (Tregs) predominantly infiltrated tissues from patients with PD, while cytotoxic CD8+ T cells were primarily found in tissues from patients who achieved SD and CR (Fig. 3G, H). Stem-like CD8+ T cells have garnered attention for their capacity to maintain long-term T-cell responses due to their stem-like properties [12]. We found that, compared with tissues from non-CR patients, tissues from CR patients had a greater infiltration of stem-like CD8+ T cells (Fig. 3H). Furthermore, CD8+ T cells infiltrating CR tissues exhibited increased expression of exhaustion markers, suggesting that these patients may benefit from ICI therapy (Fig. 3H).

We also observed that tissues from patients who achieved CR contained abundant vascular vessels (Fig. 3A, B). The vasculature in the tumor not only contributes to immunotherapy responses by facilitating lymphocyte trafficking but also supports chemotherapy efficacy by ensuring adequate drug delivery to the tumor bed [13]. To further characterize the molecular and functional properties of the endothelial vessels in PD, SD, and CR tissues, we performed GSVA of DEGs within the Endovascular CTN. The GSVA results revealed that the vascular vessels of the CR patients exhibited a more mature phenotype and a greater capacity for T/B-cell recruitment (Fig. 3I). In contrast, vascular vessels in tissues from PD patients showed lower levels of leukocyte-endothelial cell adhesion, a key process for lymphocyte extravasation. Additionally, we found that the Endovascular CTN of CR tissues displayed increased expression of lymphocyte- and adhesion molecule-related genes (Fig. 3J). Taken together, our findings suggest that high levels of lymphocytes infiltrating blood vessels, B-cell

activation, and enrichment of pro-immune-type T cells can serve as important indicators for predicting the response to neoadjuvant therapy.

TLSs are observed in patients who achieve CR

High numbers of tumor-infiltrating T cells and B cells are closely associated with the formation of TLSs, and the activation of B cells within the TME is dependent on the presence of TLSs [14]. In our study, we found that the number of tumor-infiltrating T cells was comparable across the different patient groups, while B cells were significantly enriched in the tissues from patients who achieved CR (Fig. 4A). Moreover, tissues from CR patients exhibited elevated expression levels of germinal center (GC) B cells, TLS-associated chemokines, adhesion molecules, the dendritic cell (DC) marker LAMP3, lymphotoxin signaling molecules, and HEV markers (Fig. 4A). As anticipated, signature-based analysis revealed that tissues from MIBC patients with CR showed high levels of lymph node development signals and TLS-associated signals, which were strongly colocalized with B-cell activation signals (Fig. 4B). By integrating H&E staining maps with gene expression data, we identified two distinct TLS regions in tissues from CR patients (Fig. 4C). Focusing on tissues from CR patients, which contain these TLSs, we evaluated the spatial distribution of T and B-cell according to the expression of specific cell markers (CD3 for T cells and MS4A1 for B cell). We observed that the core regions of the TLSs colocalized with both T and B cells, rather than with either T or B cells alone (Fig. 4C). The differentiation of B cells requires interactions with T cells. At the interface between the follicular and T-cell zones in secondary lymphoid organs, B cells interact with CD4+ helper T cells [15]. These ongoing interactions between T cells and B cells are critical for the maintenance of GCs. Within the GCs, the interaction between B cells and T follicular helper (Tfh) cells promotes B-cell proliferation, class switch recombination, and differentiation into antibody-producing plasma cells or GC B cells [15]. Recent studies have shown that B cells express major histocompatibility complex (MHC) class II molecules and possess the necessary machinery for antigen uptake, processing, and presentation, classifying them as professional antigen-presenting cells (APCs), akin to DCs and macrophages [16, 17]. In addition, B cells

(See figure on next page.)

Fig. 4 CCL19/CCL21 driven TLSs can be observed in treatment naïve tissue of CR patient. **A** Violin plots show the expression of TLS related genes across different response groups. **B** Spatial feature plots show the expression and distribution of TLS related signatures. **C** TLS regions were identified in treatment naïve CR tissue. **D** Immunoregulation signaling was compared in T&B cell spots between inner and outer of TLS. **E** SpaGene analysis identified ligand-receptor pairs that dominantly expressed in TLS regions. **F** IHC analysis presents TLS region in mouse tumor slides. **G** Tumor weights in different treatment groups. The difference between groups was analyzed by Student's t-tests. n = 5 mice for each group

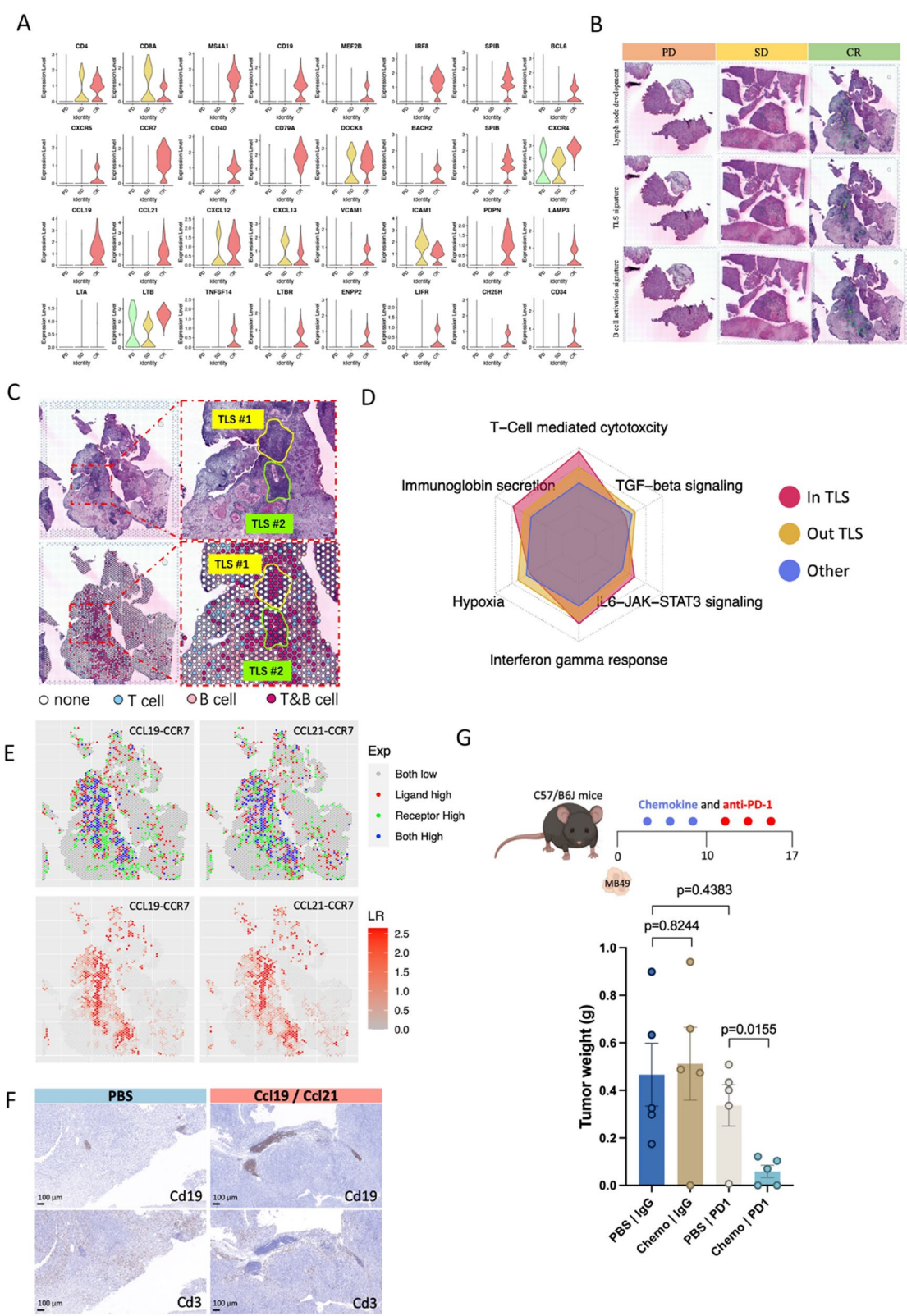


Fig. 4 (See legend on previous page.)

also express costimulatory molecules, including CD80 and CD86, which enhance T-cell activation by interacting with CD28 on T cells [16, 17]. To further explore the molecular and functional characteristics of T and B cells within TLSs, we compared T and B cell spots within and outside the TLS regions. Differential expression analysis revealed that chemokines involved in lymphocyte recruitment, as well as genes associated with B-cell activation and maturation, were more highly expressed within the TLS regions (Fig. S3A). GSEA further confirmed the increased activity of B-cell activation in T and B cell spots within the TLS regions (Fig. S3B). Furthermore, signature-based analysis showed that T cells within the TLS regions exhibited a greater cytotoxic potential, while B cells within these regions displayed characteristics consistent with antibody-secreting plasma cells. These findings suggest that the colocalization, or interaction, of T and B cells within the TLSs results in a stronger synergistic antitumor immune response (Fig. 4D).

Since lymphocyte aggregation is primarily governed by chemokine gradients and cell–cell interactions, we investigated the ligand–receptor pairs (LRPs) contributing to lymphocyte aggregation using the R package SpaGene (version 0.1.0). This analysis identified nine chemokine-mediated cell–cell communication patterns within the tissue from patients who achieved CR (Fig. S3C). Among these, we identified TLS-specific LRPs (pattern 2 in Fig. S3C). Notably, the CCL19/CCL21-CCR7, CCL5/CCL14-ACKR1, and CXCL9-CXCR3 LRP axes were among the top five TLS-associated patterns (Fig. S3D). CCL19-CCR7 and CCL21-CCR7 are well-established canonical chemokine axes that promote TLS formation [18]. We observed that CCL19/CCL21-CCR7 signaling was predominantly localized within the TLS regions (Fig. 4E). Within TLSs, CCL19+ and/or CCL21+ fibroblastic reticular cells (FRCs) guide the distribution of lymphocytes expressing the corresponding CCR7 receptors, thereby facilitating the formation of the T-cell zone formation [18, 19]. Additionally, CCL19/CCL21 recruit CCR7-expressing mature DCs, particularly LAMP3+ DCs, into the TLS regions to prime naïve T cells [18].

In the TME, CXCL9, expressed by intratumoral conventional DCs, plays a key role in recruiting stem-like

CD8+ T cells, promoting the replenishment of the effector T-cell pool [11]. Furthermore, ACKR1, expressed on the blood endothelial cells (BECs) of postcapillary venules, facilitates the abluminal-to-luminal transcytosis of chemokines, thereby promoting the extravasation of immune cells from the vasculature into the tumor bed [20]. We hypothesize that CCL5, retained at BEC junctions by ACKR1, aids immune cell extravasation, facilitating their infiltration into the TME.

Subsequently, we explored the potential of the CCL19/CCL21-CCR7 axis as a therapeutic target for MIBC. The MB49 mouse bladder carcinoma cell line was intraperitoneally (i.p.) injected into C57BL/6J mice. Starting on day 3, recombinant mouse Ccl19 and Ccl21 were administered i.p. six times every 2–3 days, and tumors were harvested on day 17. IHC analysis revealed that Ccl19/Ccl21 administration facilitated the formation of intratumoral TLSs (Fig. 4F, Fig. S4). More importantly, we observed that the delivery of Ccl19/Ccl21 enhanced the therapeutic efficacy of PD-1 inhibition, suggesting that these chemokines may serve as effective neoadjuvant therapeutic agents for MIBC (Fig. 4G).

In summary, we identified the presence of TLSs in the tumors of patients who achieved CR, which was strongly associated with high levels of CCL19 and CCL21 enrichment in the TME. Furthermore, both CCL19 and CCL21 were shown to enhance the therapeutic efficacy of immunotherapy.

TLS formation process

To gain deeper insight into TLS formation in MIBC, we conducted a detailed analysis of the Immunity/TB CTN in tissues from patients who achieved CR. The formation of TLSs is a multistep process, which involves: (1) the aggregation of lymphocytes, (2) the establishment of distinct T-cell and B-cell zones, and (3) the formation of GC-like structures within the B-cell zone [18]. Interestingly, we identified two primary distribution patterns within the Immune/TB and Immune/mixed CTNs. In the TLS region, the Immune/TB CTN was surrounded by Immune/mixed CTN and formed a follicular structure (pattern 1), while in the non-TLS region, the Immune/TB CTN was distributed around the Immune/mixed

(See figure on next page.)

Fig. 5 Changes in cellular components and signaling pathways during TLS formation. **A** Distribution of cell type niche in treatment naïve tissue of CR patient. **B** Heatmap shows the expression level of cell type signatures calculated by deconvolution method. The red star (Sig) represents the statistical significance of difference of immune. TB between two pattern groups. **C** Pseudotime analysis identifies the trajectory of expression changes in TLS-associated cytokine. **D** Heatmap shows the expression changes of different pattern specific genes during the TLS formation process. GO analysis was conducted based on these specific genes. **E** Schematic diagram of TLS and non-TLS patterns. The graph was generated by Biorender (<https://biorender.com>). **F** Spatial feature plots show the expression of nine TLS related genes. **G** Composition of the TME and the expression of nine-gene signature in TCGA-BLCA cohort calculated by the MCP-counter Z-scores

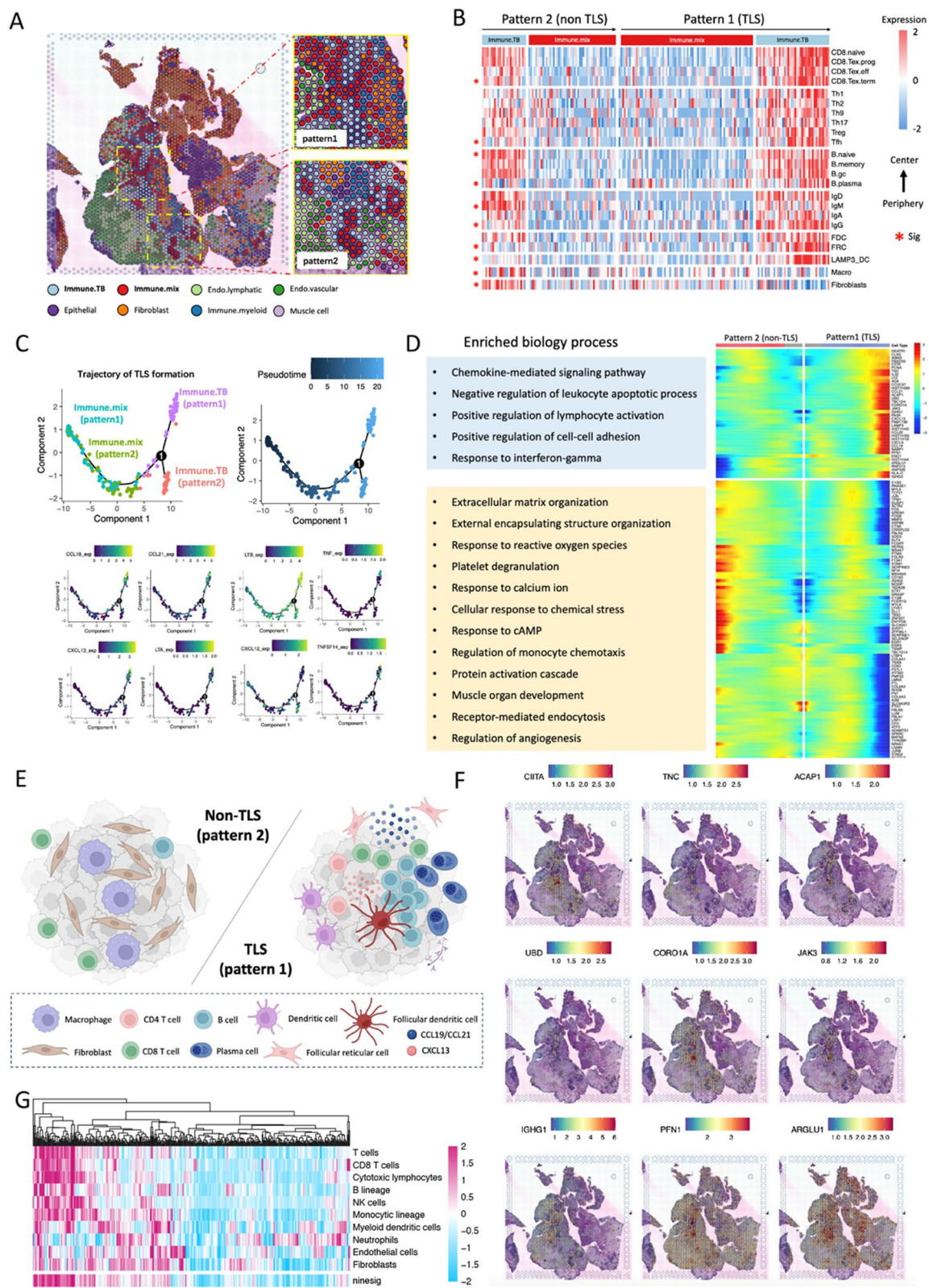


Fig. 5 (See legend on previous page.)

CTN (pattern 2) (Fig. 5A). We hypothesized whether this phenomenon represents a progression in TLS formation, i.e., if the non-TLS pattern (pattern 2) eventually transitions into the TLS pattern (pattern 1), or if these patterns represent distinct evolutionary paths for lymphocyte clusters. To test this hypothesis, we compared the cellular composition and molecular characteristics of the Immune/TB CTN between the TLS-pattern and non-TLS-pattern. Deconvolution analysis using the monocytic cell proportion (MCP)-counter method [21] further identified lymphocyte subtypes, as well as other cell types that colocalized with lymphocytes (Fig. 5B). In addition to the organized T-zone and B-zone, TLSs encompass a variety of cellular components, with Tfh cells being the most prominent. As anticipated, we observed a significant enrichment of Tfh cells within the TLS_TB regions. The interaction between B cells and Tfh cells drives immunoglobulin class-switching and affinity maturation in GCs, resulting in the generation of high-affinity, long-lived plasma cells [15] (Fig. 5B). We also noted that IgM-positive naïve B cells were predominantly found in the non-TLS region, while IgG-positive B cells and plasma cells were significantly enriched in the TLS regions (Fig. 5B). Furthermore, we identified that FRCs and follicular dendritic cells (FDCs), collectively termed lymphoid tissue organizer (LTo) cells, were significantly enriched in the pattern 1_TB (Fig. 5B). These findings align with previous reports by Jeremy Goc et al., who demonstrated that LAMP3+DCs (also referred to as DC-LAMP) are predominantly localized within the T-cell zone of TLSs [22]. Consistently, we found that LAMP3+DCs were significantly enriched in the pattern 1_TB region compared with the pattern 2_TB region. Interestingly, we also observed that terminally exhausted CD8+T cells were enriched in the pattern 1_TB region, while macrophages and fibroblasts were more abundant in the pattern 2_TB region.

To further investigate the relationship between the TLS and non-TLS patterns, we performed pseudotime analysis using Monocle2 [23]. This analysis revealed a trajectory that originated at immune spots within the Immune/mixed CTN and subsequently bifurcated into two distinct differentiation paths: one leading to the Immune/TB spots in the pattern 1 region and the other leading to Immune/TB spots in the pattern 2 region (Fig. 5C). As expected, key TLS-associated molecules were predominantly enriched along the path leading to the pattern 1 region spots (Fig. 5C). To identify the characteristic factors involved in TLS formation, we analyzed the genes whose expression changed significantly over the course of pseudotime progression. Notably, genes that were highly expressed along the TLS trajectory were involved in processes related to cell–cell communication, including

chemokine-mediated signaling, cell adhesion, and activation, highlighting the dynamic cell–cell interactions occurring during TLS formation (Fig. 5D). In contrast, the pattern 2 region branch was characterized by the enrichment of extracellular matrix (ECM) remodeling-related signaling pathways, which may inhibit lymphocyte interactions and, consequently, prevent TLS formation (Fig. 5D). Additionally, angiogenesis-related terms were significantly enriched in the pattern 2_TB region. The angiogenesis-driven immunosuppressive TME is known to lead to T-cell dysfunction, which disrupts T-B-cell interactions and inhibits TLS formation [13]. Recent studies have highlighted the role of tumor-associated macrophages (TAMs) and cancer-associated fibroblasts (CAFs) in ECM remodeling and angiogenesis [24, 25], and we hypothesize that these immunosuppressive processes mediated by TAMs and CAFs may inhibit TLS formation (Fig. 5E). Moreover, we identified several previously unreported TLS-related genes that were significantly upregulated in TLSs (Fig. 5F). The signature score, calculated using these newly identified TLS-associated genes in the TCGA-BLCA cohort, was positively correlated with the lymphocyte infiltration levels (Fig. 5G).

In summary, our results indicate that TLS formation requires not only the chemokine-mediated recruitment and cell–cell interactions of specific cell populations (such as LAMP3+DCs, Tfh cells, FRCs and FDCs) but also an immunosupportive TME (Fig. 5E). Additionally, we identified novel TLS-associated genes that are significantly correlated with immune cell infiltration in MIBC.

MIBC patients exhibit intrinsic heterogeneity within the tumor

The neoadjuvant therapies administered in this cohort included camrelizumab and gemcitabine and cisplatin. The sensitivity to immunotherapy is influenced by the immunophenotype of the tumor, whereas the sensitivity to chemotherapy is more dependent on the intrinsic characteristics of the tumor. Therefore, the selection of an appropriate therapeutic strategy necessitates a comprehensive assessment of both the immune microenvironment and the tumor characteristics.

To further investigate the tumor characteristics in responders, we conducted an analysis of the epithelial niches before and after therapy (Fig. 6A). Tumor purity scores were calculated at epithelial sites using the ESTIMATE package in R [26]. As anticipated, tumor purity in tissues from patients who achieved a CR significantly decreased following neoadjuvant therapy (Fig. 6B). To evaluate the heterogeneity of the tumor regions across different response groups, we focused on samples from Clusters 3 and 4, which exhibited high tumor purity, for further analysis. Recently, MIBC has been classified into

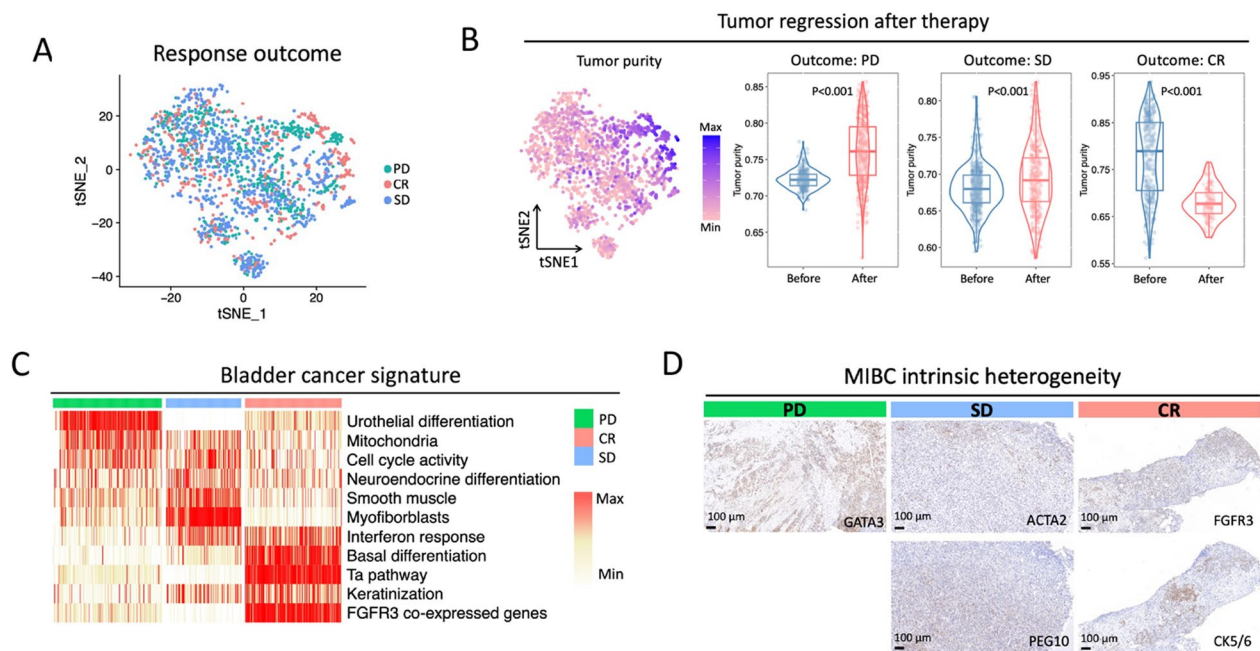


Fig. 6 Intrinsic heterogeneity of the MIBC tumors. **A** tSNE map of epithelial niche spots across different response outcomes. **B** Tumor purity and its expression levels before and after treatment. **C** Heatmap shows the expression level of MIBC subtype signature. **D** IHC analysis identified intrinsic heterogeneity of treatment naïve MIBC tissues

six consensus molecular subtypes: the luminal papillary (LumP), luminal nonspecified (LumNS), luminal unstable (LumU), stroma-rich, basal/squamous (Ba/Sq), and neuroendocrine-like (NE-like), each of which displays distinct responses to immunotherapy and chemotherapy [27]. We applied a signature-based approach to calculate consensus class-related pathway scores across various tumor sites. This analysis revealed that malignant spots in patients who achieved PD and CR exhibited elevated urothelial differentiation signals (Fig. 6C). Furthermore, malignant spots from PD patients demonstrated increased cell cycle activity, while those from CR patients showed high expression of a noninvasive Ta pathway signature and an FGFR3 coexpressed gene signature, suggesting that the PD group primarily corresponds to the LumU phenotype, while the CR group aligns with the LumP phenotypes (Fig. 6C). Interestingly, we also observed that malignant spots from CR patients displayed high levels of basal differentiation and elevated cytotoxic lymphocyte infiltration, characteristics associated with the Ba/Sq phenotype. This suggests that CR patients exhibit a combination of LumP and Ba/Sq phenotypes (Fig. 6C). In contrast, malignant spots from patients with SD expressed signals indicative of neuroendocrine differentiation, cell cycle activity, and myofibroblasts, indicating a mixture of NE-like and stromal-rich phenotypes in these patients (Fig. 6C). These findings

were further validated through IHC analysis (Fig. 6D, Fig. S5).

In summary, our study revealed distinct molecular subtype compositions within individual MIBC patients. Specifically, patients with CR in our cohort exhibited a combination of LumP and Ba/Sq tumor phenotypes, while patients with SD displayed a mixture of NE-like and stromal-rich phenotypes. These observations underscore the importance of considering tumor heterogeneity when designing precision therapies.

Discussion

Cisplatin-based neoadjuvant chemotherapy (NAC) prior to radical cystectomy remains the standard treatment for MIBC. However, a study has shown that only 30–40% of patients undergoing NAC achieve ypT0N0 disease [28]. Given the promising efficacy of immunotherapy in advanced bladder cancer, combining NAC with immunotherapy holds potential for improving survival outcomes in MIBC patients [4, 29]. Recent studies, however, have highlighted that bladder cancer encompasses a variety of histological and molecular subtypes, each of which exhibits differential sensitivities to current therapeutic modalities [30, 31]. Approximately 40% of urothelial carcinoma cases demonstrate differentiation, which can significantly affect treatment responses [30]. A post hoc analysis of the VESPER trial revealed that patients

with $\geq 50\%$ squamous cell differentiation or $\geq 50\%$ micropapillary subtype showed reduced progression-free survival (PFS) following NAC. In recent years, several molecular classifications have been developed to better stratify patients based on prognosis and therapeutic response [27, 32–34]. For instance, Robertson et al. [35] identified five distinct subtypes in the PURE01 trial, characterized by unique genomic profiles, transcriptomic signatures, and distinct TME, which influence differential responses to neoadjuvant immunotherapy. Therefore, comparing tumor samples with varying responses before and after NAC combined with immunotherapy presents an opportunity to identify key biological features that could inform more effective and personalized treatment strategies for bladder cancer patients.

In this study, we analyzed the genome-wide transcriptomic heterogeneity of patients with three distinct responses to treatment (PD, SD and CR) using ST methods. Our analysis revealed that patients with CR exhibited significantly higher levels of lymphocyte infiltration and activation. Notably, we observed that the high density of lymphocytes in CR patients led to the formation of specialized structures known as TLS. Recently, various studies have shown that the density and maturity of TLS are correlated with better responses to immunotherapy, especially ICI [18]. The presence of TLSs in tumors is often associated with the increasing of immune Infiltration [36]. Due to their lymph node-like structure and the presence of mature DCs, TLSs serve as an ideal site for T cell local priming [18]. This also explains why patients with TLSs have a better response rate to ICI therapy. In addition, the GC structures within TLS can also promote the differentiation of B cells into plasma cells. The antibodies secreted by these plasma cells can mediate tumor killing through antibody-dependent cellular cytotoxicity (ADCC) and antibody-dependent cellular phagocytosis (ADCP) [37]. Therefore, inducing the intratumoral TLS is highly effective in enhancing the sensitivity of bladder cancer to immunotherapy.

By comparing T-cell- and B-cell-dominant spots both within and outside the TLS regions, we found that spots within the TLS regions exhibited higher levels of anti-tumor signaling compared to those outside the TLS regions. This may be attributed to the closer proximity of T and B cells within the TLS, which enhances their interaction capacity and thereby promotes more effective immune functions. To further investigate the mechanisms underlying TLS formation, we conducted pseudotime analysis, mapping the pathways associated with changes in cellular components during TLS development. Our findings highlighted that the CCL19/CCL21-CCR7 axis plays a dominant role in this process, positioning CCL19 and CCL21 as promising therapeutic

targets for MIBC. Additionally, we validated the therapeutic potential of CCL19/CCL21 in mouse models. Chemokine-mediated cancer therapy is increasingly gaining attention. Generally, there are two therapeutic approaches for harnessing chemokines in cancer therapy: one is to inhibit immune-suppressive chemokines, and the other is to enhance the enrichment of inflammatory chemokines. As important inflammatory chemokines, the therapeutic strategy of CCL19/CCL21 is to increase the concentration of CCL19 and CCL21 in the tumor area through rational drug delivery methods, forming a chemokine gradient to promote greater lymphocyte infiltration. This can be achieved by delivering recombinant proteins, as employed in this study, or by using adeno-associated virus (AAV). The anti-tumor effects of CCL19 and CCL21 proteins have been validated in several pre-clinical mouse models [38, 39]. Therefore, we believe that the administration of CCL19/CCL21 recombinant protein drugs via intravenous, intravesical, and intratumoral injection could be effective in the treatment of bladder cancer. Moreover, we explored the intrinsic heterogeneity of spots of malignant cell spots and observed that a single patient could harbor multiple tumor subtypes, providing an explanation for the variable efficacy of MIBC treatments.

Our study has several limitations. The primary constraint is the limited sample size, which may introduce bias and affect the generalizability of our findings. Additionally, the inherent limitations of ST technology complicate the dissection of the TME at the single-cell resolution level, which in turn poses challenges for the analysis and interpretation of the results. To mitigate these limitations, we took measures to enhance the robustness of our study through deeper analyses and experimental validations. Despite these challenges, our research provides valuable insights and contributes to a broader clinical perspective, advancing our understanding of MIBC.

Conclusions

Our study demonstrates that patients who achieve a pCR to neoadjuvant therapy exhibit high levels of lymphocyte infiltration, which leads to the formation of TLS. A comprehensive analysis of ST data revealed that the CCL19/CCL21-CCR7 ligand-receptor pair plays a critical role in TLS formation. Findings from mouse experiments further support the potential of CCL19 and CCL21 as therapeutic targets to enhance the ICI response rate in patients with MIBC. Moreover, we identified intrinsic heterogeneity within tumors from individual patients, which may influence the response to ICI therapy.

Following these findings, we have also come up with new questions: What are the clinical methods to deliver

these chemokines to the tumor? Among intravenous injection, intravesical instillation, and intratumoral injection, which method is the most effective and the most acceptable to patients? In addition to CCL19/CCL21, what other molecules can promote the formation of tertiary lymphoid structures in bladder cancer? We will conduct more research in the future to try to address these questions.

Abbreviations

MIBC	Muscle-invasive bladder cancer
TME	Tumor microenvironment
TLS	Tertiary lymphoid structure
pCR	Pathological complete response
ICIs	Immune checkpoint inhibitors
scRNA-seq	Single-cell RNA sequencing
ISH	In situ hybridization
MERFISH	Multiple error-robust fluorescence in situ hybridization
seqFISH	Sequential fluorescence in situ hybridization
ST	Spatial transcriptomics
TURBT	Transurethral resection of bladder tumors
IV	Intravenously
RC	Radical cystectomy
CR	Complete response
FFPE	Formalin-fixed paraffin-embedded
PD	Progressive disease
SD	Stable disease
H&E	Haematoxylin and eosin
IHC	Immunohistochemical
HEVs	High endothelial venules
HVFs	High variable features
PCA	Principal component analysis
SNN	Shared nearest neighbour
GO	Gene ontology
GSVA	Gene set variation analysis
DMEM	Dulbecco's Modified Eagle Medium
FBS	Fetal bovine serum
CTN	Cell-type niche
DEGs	Differentially expressed genes
Tregs	Regulatory T cells
GC	Germinal center
DC	Dendritic cell
Tfh	T follicular helper
MHC	Major histocompatibility complex
APCs	Antigen-presenting cells
LRPs	Ligand–receptor pairs
FRCs	Follicular reticular cells
BECs	Blood endothelial cells
i.p.	Intraperitoneally
MCP	Monocytic cell proportion
FDCs	Follicular dendritic cells
LTo	Lymphoid tissue organizer
ECM	Enrichment of extracellular matrix
TAMs	Tumor-associated macrophages
CAFs	Cancer-associated fibroblasts
LumP	The luminal papillary
LumNS	Luminal nonspecified
LumU	Luminal unstable
Ba/Sq	Basal/squamous
NE-like	Neuroendocrine-like
NAC	Neoadjuvant chemotherapy
PFS	Progression-free survival
ADCC	Antibody-dependent cellular cytotoxicity
ADCP	Antibody-dependent cellular phagocytosis
AAV	Adeno-associated virus
CAMS	Chinese Academy of Medical Science

Supplementary Information

The online version contains supplementary material available at <https://doi.org/10.1186/s12967-025-06358-w>.

Supplementary Material 1: Figure S1. TSNE map shows cell type markers. Figure S2. Spatial feature plots show cell type niche score. Figure S3. TLS associated genes and pathway. Volcano plots shows differential expressed genes of T&B cell spots inside and outside the TLS regions. GSEA analysis identified the biological processes involved by differential expressed genes of T&B cell spots inside and outside the TLS regions. SpaGene analysis identified ligand-receptor pairs in treatment naïve tissue of CR patient. Figure S4. Whole pictures of IHC staining mouse slides. Figure S5. Whole pictures of IHC staining MIBC slides

Supplementary Material 2

Acknowledgements

We thank all the technical personnel at the Laboratory Animal Center, Shanxi Province Cancer Hospital, for sample handling and processing.

Author contributions

Wasilijiang Wahafu and Nianzeng Xing contributed to the study conception. Zhu Wang, Xiangpeng Kan, and Xiongjun Ye collected samples. Quan Zhou, Yuanyuan Zhao, Xihua Yang, Yongming Yang contributed to administrative, technical, or material support. Wasilijiang Wahafu and Yongming Yang performed data analysis. Nianzeng Xing supervised the project. All authors have read and approved the manuscript.

Funding

Chinese Academy of Medical Science (CAMS) Innovation Fund for Medical Sciences grant 2022-I2M-1-008 and 2023-I2M-QJ-006 to Nianzeng Xing; the Science and Technology Department Basic Research Project of Shanxi grant 20230302121 1228, and the Science and Education Cultivation Fund of the National Cancer and Regional Medical Center of Shanxi Provincial Cancer Hospital grant QH2023023 to Wasilijiang Wahafu.

Data availability

Original data are available upon reasonable request.

Declarations

Ethics approval and consent to participate

The study was approved by National Cancer Center/Cancer Hospital, Chinese Academy of Medical Sciences and Peking Union Medical College (approval #20/084-2280). All investigations carried out in this study were performed in accordance with the tenets of the Declaration of Helsinki.

Competing interests

The authors declare no competing interests.

Consent for publication

Each patient enrolled in this study provided written informed consent. All authors have read and approved the manuscript.

Author details

¹Department of Urology, National Cancer Center/National Clinical Research Center for Cancer/Cancer Hospital, Chinese Academy of Medical Sciences and Peking Union Medical College, Beijing 100021, China. ²Department of Urology, Shanxi Province Cancer Hospital/Shanxi Hospital Affiliated to Cancer Hospital, Chinese Academy of Medical Sciences/Cancer Hospital Affiliated to Shanxi Medical University, Taiyuan, Shanxi 030013, China. ³Department of Pathology, National Cancer Center/National Clinical Research Center for Cancer/Cancer Hospital, Chinese Academy of Medical Sciences and Peking Union Medical College, Beijing, 100021, China. ⁴Laboratory Animal Center, Shanxi Province Cancer Hospital/Shanxi Hospital Affiliated to Cancer Hospital, Chinese Academy of Medical Sciences/Cancer Hospital Affiliated to Shanxi Medical University, Taiyuan, Shanxi, 030013, China. ⁵Department of Pathology, Shanxi Province Cancer Hospital/Shanxi Hospital Affiliated to Cancer Hospital,

Chinese Academy of Medical Sciences/Cancer Hospital Affiliated to Shanxi Medical University, Taiyuan, Shanxi, 030013, China.

Received: 1 January 2025 Accepted: 7 March 2025

Published online: 27 March 2025

References

- Bray F, Laversanne M, Sung H, Ferlay J, Siegel RL, Soerjomataram I, Jemal A. Global cancer statistics 2022: GLOBOCAN estimates of incidence and mortality worldwide for 36 cancers in 185 countries. *CA Cancer J Clin*. 2024;74:229–63.
- Grossman HB, Natale RB, Tangen CM, Speights VO, Vogelzang NJ, Trump DL, deVere White RW, Sarosdy MF, Wood DP Jr, Raghavan D, Crawford ED. Neoadjuvant chemotherapy plus cystectomy compared with cystectomy alone for locally advanced bladder cancer. *N Engl J Med*. 2003;349:859–66.
- de Biasi AR, Villena-Vargas J, Adusumilli PS. Cisplatin-induced antitumor immunomodulation: a review of preclinical and clinical evidence. *Clin Cancer Res*. 2014;20:5384–91.
- Han S, Ji Z, Jiang J, Fan X, Ma Q, Hu L, Zhang W, Ping H, Wang J, Xu W, et al. Neoadjuvant therapy with camrelizumab plus gemcitabine and cisplatin for patients with muscle-invasive bladder cancer: a multi-center, single-arm, phase 2 study. *Cancer Med*. 2023;12:12106–17.
- Rose TL, Harrison MR, Deal AM, Ramalingam S, Whang YE, Brower B, Dunn M, Osterman CK, Heiling HM, Bjurlin MA, et al. Phase II study of gemcitabine and split-dose cisplatin plus pembrolizumab as neoadjuvant therapy before radical cystectomy in patients with muscle-invasive bladder cancer. *J Clin Oncol*. 2021;39:3140–8.
- Wang D, Liu B, Zhang Z. Accelerating the understanding of cancer biology through the lens of genomics. *Cell*. 2023;186:1755–71.
- Chen KH, Boettiger AN, Moffitt JR, Wang S, Zhuang X. RNA imaging. Spatially resolved, highly multiplexed RNA profiling in single cells. *Science*. 2015. <https://doi.org/10.1126/science.aaa6090>.
- Eng CL, Lawson M, Zhu Q, Dries R, Koulena N, Takei Y, Yun J, Cronin C, Karp C, Yuan GC, Cai L. Transcriptome-scale super-resolved imaging in tissues by RNA seqFISH. *Nature*. 2019;568:235–9.
- Vickovic S, Eraslan G, Salmen F, Klughammer J, Stenbeck L, Schapiro D, Aijo T, Bonneau R, Bergenstrahle L, Navarro JF, et al. High-definition spatial transcriptomics for in situ tissue profiling. *Nat Method*. 2019;16:987–90.
- Speiser DE, Chijioke O, Schaeuble K, Munz C. CD4(+) T cells in cancer. *Nat Cancer*. 2023;4:317–29.
- Tooley KA, Escobar G, Anderson AC. Spatial determinants of CD8(+) T cell differentiation in cancer. *Trend Cancer*. 2022;8:642–54.
- Gebhardt T, Park SL, Parish IA. Stem-like exhausted and memory CD8(+) T cells in cancer. *Nat Rev Cancer*. 2023;23:780–98.
- Huang Y, Kim BYS, Chan CK, Hahn SM, Weissman IL, Jiang W. Improving immune-vascular crosstalk for cancer immunotherapy. *Nat Rev Immunol*. 2018;18:195–203.
- Fridman WH, Meylan M, Pupier G, Calvez A, Hernandez I, Sautes-Fridman C. Tertiary lymphoid structures and B cells: an intratumoral immunity cycle. *Immunity*. 2023;56:2254–69.
- Suan D, Sundling C, Brink R. Plasma cell and memory B cell differentiation from the germinal center. *Curr Opin Immunol*. 2017;45:97–102.
- Kwak K, Akkaya M, Pierce SK. B cell signaling in context. *Nat Immunol*. 2019;20:963–9.
- Laumont CM, Nelson BH. B cells in the tumor microenvironment: multifaceted organizers, regulators, and effectors of anti-tumor immunity. *Cancer Cell*. 2023;41:466–89.
- Sautes-Fridman C, Petitprez F, Calderaro J, Fridman WH. Tertiary lymphoid structures in the era of cancer immunotherapy. *Nat Rev Cancer*. 2019;19:307–25.
- Barone F, Gardner DH, Nayar S, Steinthal N, Buckley CD, Luther SA. Stromal fibroblasts in tertiary lymphoid structures: a novel target in chronic inflammation. *Front Immunol*. 2016;7:477.
- Torphy RJ, Yee EJ, Schulick RD, Zhu Y. Atypical chemokine receptors: emerging therapeutic targets in cancer. *Trend Pharmacol Sci*. 2022;43:1085–97.
- Becht E, Giraldo NA, Lacroix L, Buttard B, Elarouci N, Petitprez F, Selves J, Laurent-Puig P, Sautes-Fridman C, Fridman WH, de Reynies A. Estimating the population abundance of tissue-infiltrating immune and stromal cell populations using gene expression. *Genome Biol*. 2016;17:218.
- Goc J, Germain C, Vo-Bourgeois TK, Lupo A, Klein C, Knockaert S, de Chaisemartin L, Ouakrim H, Becht E, Alifano M, et al. Dendritic cells in tumor-associated tertiary lymphoid structures signal a Th1 cytotoxic immune contexture and license the positive prognostic value of infiltrating CD8+ T cells. *Cancer Res*. 2014;74:705–15.
- Qiu X, Mao Q, Tang Y, Wang L, Chawla R, Pliner HA, Trapnell C. Reversed graph embedding resolves complex single-cell trajectories. *Nat Method*. 2017;14:979–82.
- Caligiuri G, Tuveson DA. Activated fibroblasts in cancer: perspectives and challenges. *Cancer Cell*. 2023;41:434–49.
- Kloosterman DJ, Akkari L. Macrophages at the interface of the co-evolving cancer ecosystem. *Cell*. 2023;186:1627–51.
- Yoshihara K, Shahmoradgoli M, Martinez E, Vegesna R, Kim H, Torres-Garcia W, Trevino V, Shen H, Laird PW, Levine DA, et al. Inferring tumour purity and stromal and immune cell admixture from expression data. *Nat Commun*. 2013;4:2612.
- Kamoun A, de Reynies A, Allory Y, Sjodahl G, Robertson AG, Seiler R, Hoadley KA, Groeneveld CS, Al-Ahmadie H, Choi W, et al. A consensus molecular classification of muscle-invasive bladder cancer. *Eur Urol*. 2020;77:420–33.
- Iyer G, Tully CM, Zabor EC, Bochner BH, Dalbagni G, Herr HW, Donat SM, Russo P, Ostrovskaya I, Regazzi AM, et al. Neoadjuvant gemcitabine-cisplatin plus radical cystectomy-pelvic lymph node dissection for muscle-invasive bladder cancer: a 12 year experience. *Clin Genitourin Cancer*. 2020;18:387–94.
- Galsky MD, Daneshmand S, Izadmehri S, Gonzalez-Kozlova E, Chan KG, Lewis S, Achkar BE, Dorff TB, Cetnar JP, Neil BO, et al. Gemcitabine and cisplatin plus nivolumab as organ-sparing treatment for muscle-invasive bladder cancer: a phase 2 trial. *Nat Med*. 2023;29:2825–34.
- Day E, Gavira J, Tapia JC, Anguera G, Maroto P. What about variant histologies in bladder cancer? *Eur Urol Focus*. 2024;10:227–30.
- Necchi A, Raggi D, Gallina A, Ross JS, Fare E, Giannatempo P, Marandino L, Colecchia M, Luciano R, Bianchi M, et al. Impact of molecular subtyping and immune infiltration on pathological response and outcome following neoadjuvant pembrolizumab in muscle-invasive bladder cancer. *Eur Urol*. 2020;77:701–10.
- Choi W, Porten S, Kim S, Willis D, Plimack ER, Hoffman-Censits J, Roth B, Cheng T, Tran M, Lee IL, et al. Identification of distinct basal and luminal subtypes of muscle-invasive bladder cancer with different sensitivities to frontline chemotherapy. *Cancer Cell*. 2014;25:152–65.
- Robertson AG, Kim J, Al-Ahmadie H, Bellmunt J, Guo G, Cherniack AD, Hinoue T, Laird PW, Hoadley KA, Akbani R, et al. Comprehensive molecular characterization of muscle-invasive bladder cancer. *Cell*. 2017;171(540–556): e525.
- Seiler R, Ashab HAD, Erho N, van Rhijn BWG, Winters B, Douglas J, Van Kessel KE, Fransen van de Putte EE, Sommerlad M, Wang NQ, et al. Impact of molecular subtypes in muscle-invasive bladder cancer on predicting response and survival after neoadjuvant chemotherapy. *Eur Urol*. 2017;2017(72):544–54.
- Robertson AG, Meghani K, Cooley LF, McLaughlin KA, Fall LA, Yu Y, Castro MAA, Groeneveld CS, de Reynies A, Nazarov VI, et al. Expression-based subtypes define pathologic response to neoadjuvant immune-checkpoint inhibitors in muscle-invasive bladder cancer. *Nat Commun*. 2023;14:2126.
- Schumacher TN, Thommen DS. Tertiary lymphoid structures in cancer. *Science*. 2022. <https://doi.org/10.1126/science.abf9419>.
- Fridman WH, Meylan M, Petitprez F, Sun CM, Italiano A, Sautes-Fridman C. B cells and tertiary lymphoid structures as determinants of tumour immune contexture and clinical outcome. *Nat Rev Clin Oncol*. 2022;19:441–57.
- Delvecchio FR, Fincham REA, Spear S, Clear A, Roy-Luzarraga M, Balkwill FR, Gribben JG, Bombardieri M, Hodivala-Dilke K, Capasso M, Kocher HM. Pancreatic cancer chemotherapy is potentiated by induction of

tertiary lymphoid structures in mice. *Cell Mol Gastroenterol Hepatol*. 2021;12:1543–65.

39. Zhang Y, Liu G, Zeng Q, Wu W, Lei K, Zhang C, Tang M, Zhang Y, Xiang X, Tan L, et al. CCL19-producing fibroblasts promote tertiary lymphoid structure formation enhancing anti-tumor IgG response in colorectal cancer liver metastasis. *Cancer Cell*. 2024;42(1370–1385): e1379.

Publisher's Note

Springer Nature remains neutral with regard to jurisdictional claims in published maps and institutional affiliations.